A single-mask thermal displacement sensor in MEMS

2011 J. Micromech. Microeng. 21 074007

(http://iopscience.iop.org/0960-1317/21/7/074007)

J. Micromech. Microeng. **21** (2011) 074007 (12pp) doi:10.1088/0960-1317/21/7/074007

A single-mask thermal displacement sensor in MEMS

B Krijnen[1,2], R P Hogervorst[1,4], J W van Dijk[1,2], J B C Engelen[3], L A Woldering[3], D M Brouwer[1,2], L Abelmann[3] and H M J R Soemers[2]

[1] DEMCON Advanced Mechatronics, Oldenzaal, The Netherlands
[2] Mechanical Automation Department, IMPACT Institute, University of Twente, Enschede, The Netherlands
[3] Transducers Science and Technology Department, MESA+ Institute for Nanotechnology, University of Twente, Enschede, The Netherlands

E-mail: bram.krijnen@demcon.nl

Received 23 December 2010, in final form 25 March 2011
Published 22 June 2011
Online at stacks.iop.org/JMM/21/074007

Abstract
This work presents a MEMS displacement sensor based on the conductive heat transfer of a resistively heated silicon structure towards an actuated stage parallel to the structure. This differential sensor can be easily incorporated into a silicon-on-insulator-based process, and fabricated within the same mask as electrostatic actuators and flexure-based stages. We discuss a lumped capacitance model to optimize the sensor sensitivity as a function of the doping concentration, the operating temperature, the heater length and width. We demonstrate various sensor designs. The typical sensor resolution is 2 nm within a bandwidth of 25 Hz at a full scale range of 110 μm.

(Some figures in this article are in colour only in the electronic version)

1. Introduction

The trend towards smaller and more accurate positioning systems stimulates the use of MEMS applications. Examples of such accurate positioning systems have already existed for a long time in MEMS. Two examples are (digital) light processing [1, 2] and the use of cantilevers in atomic force microscopy [3]. Actuators in combination with flexure-based stages are able to reach positioning accuracies of several nanometers. Still, accurate positioning is limited by many factors, such as drift, external disturbances and load forces. Adding feedback control, and thus a position sensor, can enhance the performance of positioning systems.

Position and acceleration sensing in MEMS is often based on the varying electrical capacitance between a static reference and an actuated stage [4–6]. The disadvantage of accurate and long-range capacitive displacement sensors is the large required wafer surface area. Some alternative sensors use integrated optical waveguides [7], the piezoresistive effect [8, 9] or varying thermal conductance [10–12]. Lantz *et al* have demonstrated a thermal displacement sensor achieving nanometer resolution over a 100 μm range [10]. However, this sensor is produced in two separate wafers and therefore precision assembly was needed to fabricate it together with the stage. We found a way to integrate a thermal displacement sensor with an actuated and flexure-based stage in the device layer of a silicon-on-insulator (SOI) wafer. Design, fabrication and experimental validation of the sensor are presented in this work.

The integration of sensor and actuator in a single layer of silicon has multiple advantages. It obeys several design principles for precision manipulation [13]; contactless sensing and actuation do not introduce friction and hysteresis. Without the assembly of separate components, misalignments are avoided. Overconstraints in a monolithic device layer are less likely to lead to unpredictable system behaviour [14]. We succeeded in integrating the sensor without any modification of the process for the fabrication of the electrostatic actuators and the flexure-based stage. The complete device is designed to be fabricated using only one mask.

The basic design of one of the heaters of the sensor is shown in figure 1. Wire bonds are connected to the bondpads

[4] R P Hogervorst did his master assignment at DEMCON Advanced Mechatronics; during the project he was a student at the Department of Precision and Microsystems Engineering, Delft University, Delft, The Netherlands.

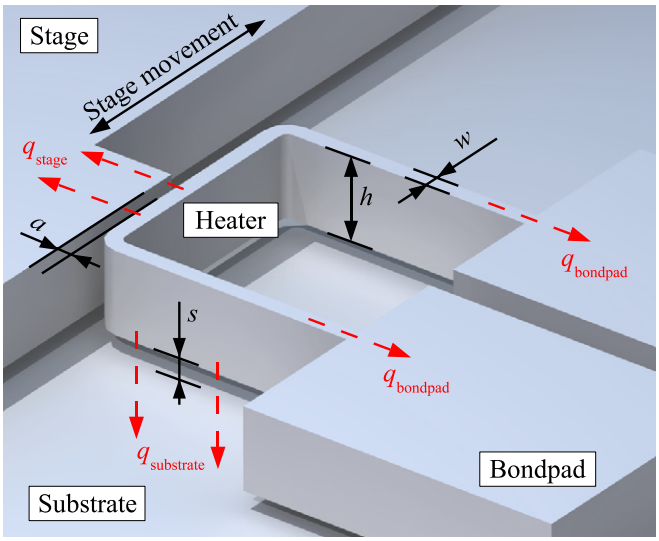

Figure 1. Schematic overview of a single heater with its dimensions and conductive heat flows (dashed red arrows). The heater height is given by h, the heater width is given by w, the air gap towards the stage by a and the air gap towards the substrate by s. The heater consists of two parts: the sensing part, which is parallel to the stage, and the heater legs, which are perpendicular to the stage. Heat conduction dominates the heat transport in the sensor. Conduction inside the silicon heater structure towards the bondpads is labelled q_{bondpad}, the conductive heat flow towards the stage is given by q_{stage} and the heat flow towards the substrate is given by $q_{\text{substrate}}$. The stage will be perforated for fabrication.

to supply an electrical current. The silicon heater is resistively heated due to the supplied electrical power. When the stage is overlapping the heater, heat is conducted from the heater to the stage, q_{stage}, through the thin layer of air, a. A large stage overlap results in efficient cooling of the heater and therefore its temperature will decrease. The resulting decrease in electrical resistance can be measured, since the electrical resistivity of silicon is highly dependent on the temperature. Thus, the electrical resistance of the heater is a measure of the position of the stage. A differential sensor configuration is chosen to make the sensor less sensitive to changes common to both heaters, such as ambient temperature and air humidity. This differential configuration is shown in figure 2.

In section 2, we will show a lumped capacitance model of the sensor. The model will be used to design and optimize the sensor. The integration of the sensor with a flexure-based stage and electrostatic comb-drive actuation is described in section 3. Fabrication will be discussed in section 4. Finally, measurements of the sensor output, noise and time constants are given in section 5.

2. Modelling and model verification

In this section, we will describe the lumped capacitance model of the sensor. The model is used to describe the temperature profile over the heaters and the heat flows in the sensor. Subsequently, the model is used to optimize the sensor sensitivity as a function of the doping concentration, the

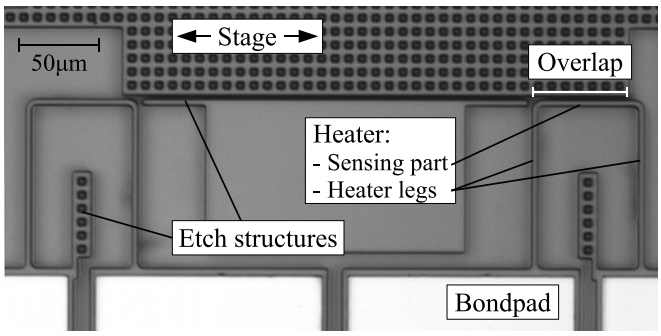

Figure 2. Top view: optical microscope image of a fabricated sensor with the actuated stage in its rightmost position. The electrostatic comb-drive actuators are outside the image. The sensor consists of two heaters. Each heater structure consists of a sensing part, two heater legs and two bondpads for mechanical and electrical connection. The heater on the right has maximum overlap with the stage, and the heater on the left has minimum overlap with the stage. 'Etch structures' are incorporated to increase the DRIE quality. The heater leg length is 100 μm and the sensing part has a length of 60 μm.

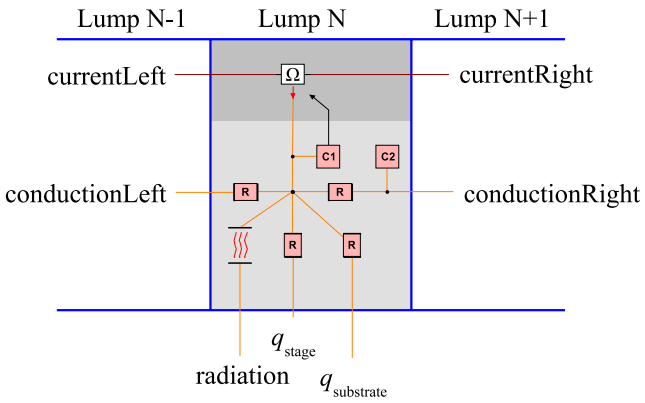

Figure 3. One of the elements of the thermal sensor model. The top of the diagram shows the electrical resistance (Ω). The thermal capacity C1 is connected to multiple thermal conductivities (R). A negligible thermal capacity C2 is added to prevent algebraic loops and the resulting increase in simulation time. Radiation is added, since it will play a role at high heater temperatures.

heater dimensions and the operating mode and temperature. The sensitivity due to variation in heater dimensions and operating temperature is validated using measurements.

2.1. Lumped capacitance model

A dynamic multiphysics model is created of the thermal sensor in 20-sim [15]. The created model is a lumped capacitance model, which divides the heater structure into a discrete number of elements [16]. Each element has a single temperature. One of the model elements is shown in figure 3. The element consists of a heat capacitance (C1) coupled to an electrical resistance (Ω). The temperature of the heat capacitance determines the electrical resistance, which in turn determines the dissipated power in the heater element. The thermal capacitance of silicon is modelled temperature dependent, according to [17]. The

temperature-dependent electrical resistance of the silicon heaters is the basic quantity through which the stage position is measured. The temperature-dependent electrical resistivity will be described in section 2.2.

Heat transport in the sensor will take place due to conduction, convection and radiation. Conduction occurs inside the silicon heater structure towards the bondpads and through the air towards the stage and the substrate, as shown in figure 1. The equation for conductive heat transfer is

$$q = \frac{\Delta T}{R_T}, \tag{1}$$

where q is the heat flow, ΔT is the difference in temperature and R_T is the thermal resistance. The thermal resistance is given by

$$R_T = \frac{l}{kA}, \tag{2}$$

where k is the thermal conductivity of the material, l is the length over which the heat transfer occurs and A is the area through which the heat transfer occurs. Both l and A are geometry and orientation dependent. The thermal conductivities of silicon and air are a function of the temperature. They are modelled according to [18] and [19], respectively.

Convection does not play a significant role in the heat transport due to the small surface area of the heated structures. Radiation increases to the fourth power with the heater temperature, and at 900 K the heat transfer due to radiation is around 2% of the total heat transfer. Radiation with an emissivity factor of 0.65 is included in the model. The emissivity factor of 0.65 takes temperature dependence as well as surface roughness of the silicon structures into account [20].

The effect of heat conduction towards the air is examined using the finite element modelling software COMSOL Multiphysics [21]. A bounding box is placed around the heater structure and underlying substrate layer. Two different boundary conditions are applied: thermal insulation and heatsink. Simulations show that when the air layer is thicker than 100 μm, the heater temperature varies by only 0.1 K for different boundary conditions. This means that the heat will flow only towards the substrate layer and the 100 μm thick air layer around the heater will function as a thermal insulation layer. In the design of the system, trenches as wide as possible are chosen to avoid heat flow through the air towards other structures in the device layer. The additional conductive heat flow towards the substrate layer is also examined using COMSOL Multiphysics. This showed that the heat conduction from the heater towards the underlying substrate is underestimated, roughly by a factor 5, when using only the heater width and the substrate gap thickness. This is caused by extra heat conduction from the sidewalls of the heaters towards the substrate.

An effective width w_{eff} is determined empirically to compensate for the additional heat flow towards the substrate. The effective width is based on the actual heater width w, the heater height h and the substrate gap thickness s,

$$w_{\text{eff}}(w, h, s) = w + w_a(h) f(s). \tag{3}$$

The additional width w_a as a function of the heater height h as well as the correction factor f as a function of the substrate gap s are approximated by a Taylor expansion,

$$w_a(h) = 1.50 \times 10^8 h^3 - 1.65 \times 10^4 h^2 + 5.95 \times 10^{-1} h + 6.99 \times 10^{-6} \tag{4}$$

$$f(s) = -2.15 \times 10^{10} s^2 + 3.49 \times 10^5 s + 1.32 \times 10^{-1}. \tag{5}$$

The effective width w_{eff} instead of the actual heater width w is used to calculate the heat flow towards the substrate. The basic equations for conductive heat transfer can be applied again, (1) and (2).

A model with 5 elements for each leg of the heater and 13 elements for the sensing part of the heater proved to be sufficient. Convergence was checked by using the same model with twice the amount of elements. COMSOL was used to verify the response of the sensor for several configurations. The model is used to gain more insight in the heat flow balance and temperature profile over the heaters and for optimization of the sensor design.

2.2. Resistivity and doping concentration

An important property in the lumped capacitance model is the resistivity of silicon as a function of temperature. A model for the temperature-dependent electrical resistivity of silicon with various doping species is given in [18]. The intrinsic carrier concentration determines the majority and minority carrier concentrations and is given in [22],

$$n_i(T) = K\sqrt{N_c N_v}\left(\frac{T}{T_0}\right)^{3/2} \exp\left(-\frac{E_g(T)}{2k_B T}\right) \tag{6}$$

where T_0 is 300 K, $N_c = 2.8 \times 10^{19}$ cm^{-3} denotes the effective density of states for electrons in the conduction band, $N_v = 1.04 \times 10^{19}$ cm^{-3} denotes the effective density of states for holes in the valence band at T_0, E_g is the band-gap energy as a function of the temperature and k_B is the Boltzmann constant. An empirical value for $K \simeq 3.0$ is used to correct the intrinsic carrier concentration n_i as a function of temperature, as described in [22].

The mobility of the charge carriers is limited due to impurity scattering and due to phonon scattering. The mobility of the charge carriers due to phonon scattering as a function of temperature is

$$\mu_{ps} = \mu_{L0}\left(\frac{T}{T_0}\right)^{p_{ps}}\left(\frac{m_e}{m}\right)^{5/2}, \tag{7}$$

where $\mu_{L0} = 1600$ cm^2 V^{-1} s^{-1} is the lattice mobility at T_0, $m_e = 0.33$ is the effective electron mass and $m = 0.55$ is the effective charge carrier mass for holes. The phonon scattering exponent p_{ps} for boron doping ranges roughly from 1.5 to 2.2 in the literature [18, 23, 24]. In our resistivity model, a phonon scattering exponent p_{ps} of 1.90 gives the best fit. For two boron doping concentrations, 3.5×10^{18} cm^{-3} and 4.7×10^{18} cm^{-3}, the theoretical model of the silicon resistivity is given together with the measured data in figure 4. The measured data fit well with the theoretical model.

The resistivity curves are used in the lumped capacitance model to examine the influence of the doping concentration

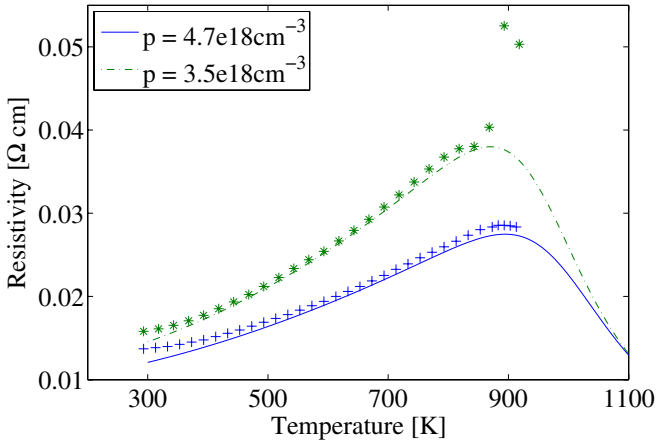

Figure 4. Resistivity model and measured data of highly boron doped silicon, with doping concentrations 3.5×10^{18} cm^{-3} and 4.7×10^{18} cm^{-3}, as a function of the temperature. Fit parameters used in the model are $p_{ps} = 1.90$ and $K = 3.0$ [22]. The aluminium wire bonds that connect the structures in a 4-point measurement setup melt around 900 K, which explains the deviated measurement results at these high temperatures.

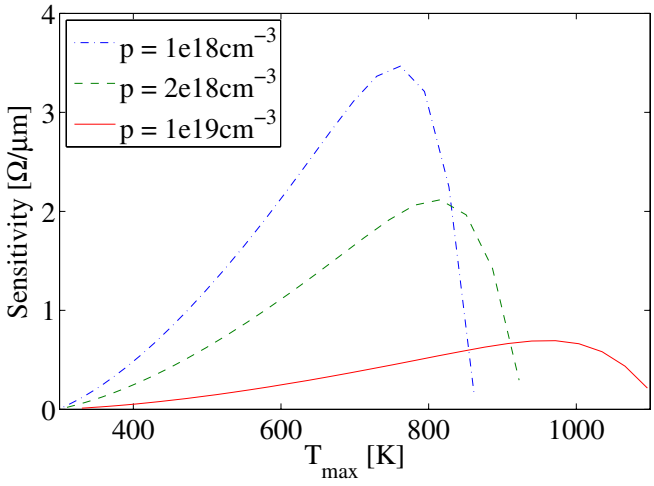

Figure 5. For a given maximum temperature at minimum overlap, the sensitivity is plotted for different doping concentrations. The heaters used in this simulation have the following dimensions: heater width and air gap 3 μm, heater length 610 μm (sensing part 130 μm and legs 240 μm), heater height 50 μm and substrate gap 3 μm.

in the device layer of the SOI wafer on the sensitivity of the sensor. In a differential configuration, the resistance change as a function of the stage overlap is roughly linear. Therefore, the resistance change from maximum to minimum overlap, divided by the stroke from maximum to minimum overlap, is a good number for the sensor sensitivity in $\Omega\ \mu\text{m}^{-1}$. To decrease boundary effects on the transition from the sensing part to the heater legs, the sensing part is designed slightly longer than the required stroke.

The sensitivity of the sensor as a function of the maximum heater temperature at minimum overlap is shown for several doping concentrations in figure 5. At a low operating temperature, the sensitivity of the sensor is restricted by the small change in temperature when going from minimum to maximum overlap. At a high operating temperature, close to the maximum resistivity, the sensitivity is restricted by the slope in the resistivity curve, which determines the resistance change as a function of the temperature change from minimum to maximum overlap.

The sensitivity of the sensors increases for lower doping concentrations. This is a direct result of the steeper slope in the resistivity curve at these lower doping concentrations (figure 4). The peak in the resistivity curve is located at a lower temperature for lower doping concentrations. This explains why the sensitivity curve for lower doping concentrations has its maximum at lower temperatures.

A lower doping concentration leads to a higher electrical resistance of the heater structures. Therefore, more intrinsic thermal Johnson–Nyquist noise will occur, which might be a problem. For the examined heater dimensions and doping concentrations, the intrinsic thermal Johnson–Nyquist does not exceed 2 μV, for a bandwidth of 1 kHz and an average heater temperature of 1000 K. Therefore, we conclude that Johnson–Nyquist noise is negligible compared with other noise sources in our sensor (also see section 5.2).

A lower limit for the doping concentration is based on the increasing electrical resistance of the comb-drive actuators when decreasing the doping concentration. This will result in higher electrical time constants of the comb-drive actuators, which can cause pull-in at high frequency actuation. For our system, a minimum doping concentration of 1×10^{16} cm^{-3} is still acceptable.

2.3. Temperature profile and power flow balance

This section will describe the temperature profile over the heaters and the power flow balance in the sensor for varying stage overlap. When the stage is at a fixed position, the power flows in the sensor should be in an equilibrium situation; the supplied electrical power must be equal to the heat flow from the heaters towards the environment. The power flow balance is dependent on the stage overlap. When the stage is in front of the heater structure (maximum overlap), this results in a lower heater temperature and therefore a lower heater resistance. Due to the lower resistance, more electrical power will be dissipated in the heater. This effect can be seen in the sum of the power flows in table 1. When the stage moves in front of the heater, more power will flow towards the stage. As a result, the heater will cool down and the power flows towards bondpads and substrate will decrease. Table 1 shows the power flow balance in the sensor for maximum, half and minimum overlap with the stage. A constant voltage of 8.3 V is applied to reach a maximum temperature of 600 K at minimum overlap. The differential sensor dissipates a more or less constant amount of power, independent of stage position. When the stage is in one of its outer positions, one of the heaters will have minimum overlap and one of the heaters will have maximum overlap. The power dissipation in this case is 80 mW + 84 mW = 164 mW. When the stage is in neutral position, both heaters will

Table 1. Calculated power flow balance in the heaters for maximum, half and minimum stage overlap. The heaters in this simulation have the following dimensions: heater width and air gap 3 μm, heater length 610 μm (sensing part 130 μm and legs 240 μm), heater height 50 μm and substrate gap 3 μm. The doping concentration is 3.5×10^{18} cm^{-3}. A constant voltage of 8.3 V was applied to the heaters.

	Maximum overlap (mW)	Half overlap (mW)	Minimum overlap (mW)
Bondpads	55	56	57
Stage	14	8	2
Substrate	15	18	21
Radiation	0	0	0
Sum	84	82	80

have half overlap and the total power dissipation will be 82 mW + 82 mW = 164 mW.

The difference in power flow from the heater to the stage q_{stage} between maximum and minimum overlap results in the temperature change in the heater. The power flows towards bondpads q_{bondpad} and substrate $q_{\text{substrate}}$ can be seen as power loss. Most of the power in the sensor will flow through the silicon heater structure towards the bondpads. This power flow is a direct result of the high thermal conductivity of silicon compared to that of air. By decreasing the heater width, the ratio between the power flow towards the bondpads and the power flow towards the stage will change, resulting in a more sensitive sensor. This effect will be discussed in section 2.4. Decreasing the heater height, which is in fact the thickness of the device layer of the SOI wafer, will have less effect on the sensor sensitivity, since it will reduce the thermal conduction to the bondpads as well as the thermal conduction towards the stage.

For the same sensor configuration used to determine the power flow balance (table 1), the modelled temperature profile over the heater for different stage overlaps is shown in figure 6. At minimum overlap, the heater structure will reach the highest temperature. In this case, the maximum temperature is limited to 600 K. When the stage partially overlaps the heater structure, the heater structure cools down and the temperature profile becomes asymmetric. Eventually, when the stage is completely in front of the heater structure, the maximum temperature of the heater structure has been decreased to 522 K. The temperature profile is roughly symmetric again. As a result of this temperature change, the heater resistance will decrease from 840 to 790 Ω, which is approximately −6% of the initial resistance.

Due to its elevated temperature, considerable thermal expansion of the sensor structures is expected. The heater legs as well as the sensing part will expand, which results in outward bending of the heater legs and bending of the sensing part towards the stage. Finite element simulations using COMSOL showed a reduction in the air gap between the heater and the stage of 150 nm for a maximum heater temperature of 700 K. This results in a higher sensor sensitivity and extra nonlinearity. In the calibration of the sensor output voltage with respect to the displacement, the effect of thermal expansion is compensated for.

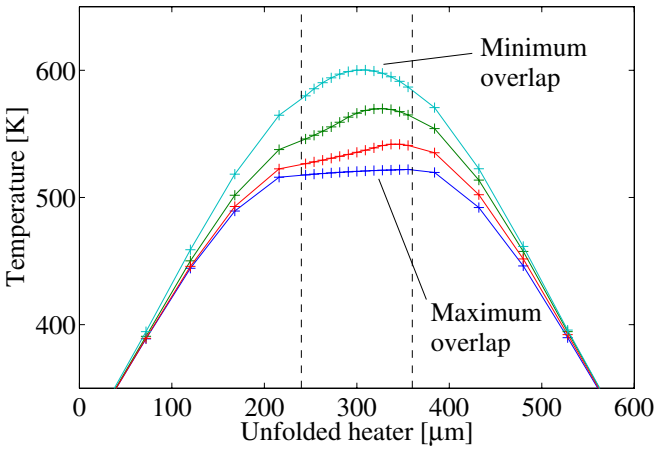

Figure 6. The modelled temperature profile over the heaters is a function of the stage overlap. The heater, sensing part and legs, is unfolded over the x-axis. The sensing part of the heater is in between 240 μm and 360 μm (vertical dashed lines). The maximum temperature is 600 K at minimum overlap and 522 K at maximum overlap. The curves in between correspond with the temperature profiles of 36% and 73% overlap.

In the chosen geometry with relatively compliant heater legs, compressive forces due to the thermal expansion of the sensing part of the heater at an operating temperature of 700 K are at least 100 times lower than the force required for buckling of the sensing part. If the sensing part is too rigidly clamped or the sensing part is very thin, buckling might occur. Since buckling will probably cause mechanical as well as electrical failure, this is a situation that must be avoided.

2.4. *Influence of heater dimensions*

The dimensions of the heaters will have an influence on the sensitivity of the sensor. The height of the heaters is the same as the thickness of the device layer of the SOI wafer. For a device layer thickness of 50 μm, the optimum in heater length and width is modelled. The minimum length of the sensing part is determined by the required stroke of the stage; only the length of the legs of the heater is varied. The sensor sensitivity as a function of the leg length is shown in figure 7 (top). The influence of the heater leg length is validated by measurements using heaters with three different leg lengths: 100 μm, 240 μm and 400 μm. The fabrication process puts restrictions on the minimum width of the heaters. Two heater widths are tested, 2 μm and 3 μm. The measurement results are shown together with the simulation results in figure 7 (bottom). On the vertical axis, the resistance change of a single heater from minimum to maximum overlap is given. The width of the designed structures is 2 μm and 3 μm. The produced structures do have an additional width of approximately 0.3 μm, as shown by scanning electron micrographs. The difference between the designed and fabricated widths is probably caused by the resist developing step after photolithography in the fabrication process. Consequently, the air gaps towards the stage decrease to 2.7 μm. The simulation results are compensated for this effect.

The simulation data show that there exists an optimum in the leg length, but the variation in leg length does not result in

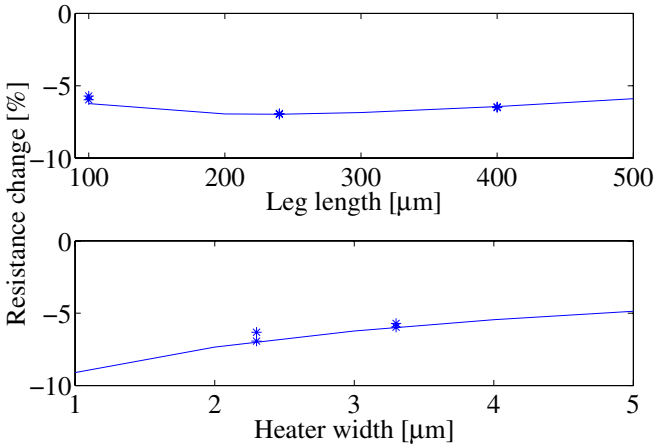

Figure 7. The resistance change from minimum to maximum overlap of a single heater structure as a function of variation in leg length (top) and heater width (bottom) is modelled (lines) and measured (stars). In the simulation, the maximum temperature at minimum overlap is set to 600 K; in the measurement, this is realized by increasing the voltage until the same resistance change as in the model to reach 600 K is measured.

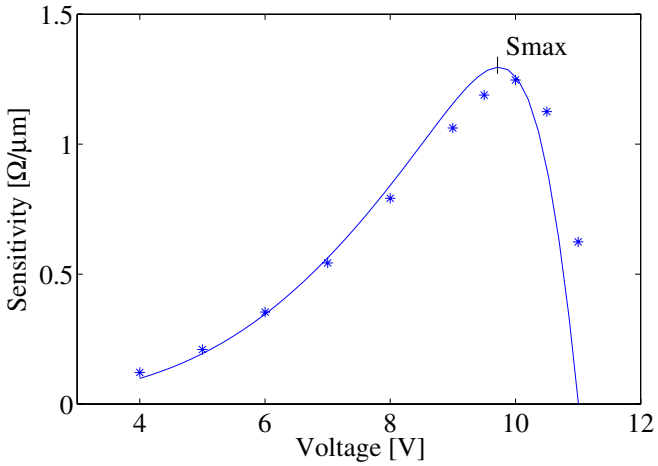

Figure 8. The sensitivity of the sensor is highly dependent on the applied voltage set point. The continuous line gives the simulation data, and the measurements are indicated by stars. The heaters in this sensor have the following dimensions: heater width 3.3 μm, air gap 2.7 μm, heater length 350 μm (sensing part 150 μm and legs 100 μm), heater height 25 μm and substrate gap 3 μm. The doping concentration in this simulation is 4.7×10^{18} cm^{-3}.

large changes in the sensitivity. For a sensor with heater width and air gap 3 μm, heater height 50 μm, substrate gap 3 μm and doping concentration 3.5×10^{18} cm^{-3}, the optimum leg length is 240 μm. The existence of an optimum in leg length can be explained by looking at the power flows from the heaters towards the substrate and towards the bondpads. At a fixed temperature of the heater and with a fixed overlap, for short heater legs the power flow towards the bondpads will increase due to a lower thermal resistance towards the bondpads. For long heater legs, the power flow towards the substrate will increase due to a large area underneath the sensor. Both of these power flows can be seen as a loss in sensitivity. In the simulation, a maximum temperature at minimum overlap of 600 K was chosen. In the measurement, this was realized by increasing the voltage until the same resistance change as in the model was measured to reach 600 K. The measurements of the leg length variation indeed show that there exists an optimum in leg length. The exact location of the optimum cannot be obtained from this limited number of measurements. The measured resistance change from minimum to maximum overlap (with respect to minimum overlap) of a single heater for a leg length of 240 μm is -6.95%, on average over two heaters. For 100 μm, the resistance change is -5.84% and for 400 μm the resistance change is -6.48%.

The effect of the heater width is also simulated and validated using measurements (see figure 7 (bottom)). The simulation clearly shows that a lower heater width will result in a higher resistance change when going from minimum to maximum overlap. For two heater widths, the resistance change is measured; a heater width of 2.3 μm gives an average resistance change of -6.62% and a heater width of 3.3 μm gives an average resistance change of -5.84%.

A large variation in the measurements at 2.3 μm width is shown in figure 7. We propose that this is caused by irregularities in the production process when fabricating thinner structures. Structures with a designed width of 2 μm and less are actually outside the window of our fabrication process, because we cannot fabricate photolithographic masks with smaller features. Although there is a fairly large variation in the measurement results for a heater width of 2.3 μm, the accuracy of the lumped capacitance model is within 10% with respect to changes in heater width and heater leg length.

2.5. Operating mode and set point

The lumped model of the thermal displacement sensor is used to investigate the influence of the applied voltage on the sensor sensitivity. Figure 8 shows that the sensitivity is highly dependent on the applied voltage to the heaters. The simulation data are validated using measurements. The sensitivity curve shown here is closely related to the sensitivity curve as a function of operating temperature, shown in figure 5, since a higher applied voltage will result in a higher temperature of the heaters.

In the simulations, the maximum sensitivity $S_{\max}$ is 1.30 Ω μm^{-1} at a supply voltage of 9.7 V. In our measurement, the maximum sensitivity is slightly lower, 1.25Ω μm^{-1}, at a supply voltage of 10 V. In general, the measured sensitivity values occur at a higher supply voltage than in the simulation. This causes the largest deviation at high operating voltages. The accuracy of the model is within 10% with respect to the measured values on the positive slope of the sensitivity curve.

An explanation for the deviation between the simulation and the measurements might be that the maximum temperature in the measurement is lower than in the simulation, causing a shift in the optimum supply voltage. A possible cause for the lower maximum temperature is a resistance in series with the MEMS heater structures, for instance on the wire bond to silicon interface. This series resistance will cause the effective voltage over the heater structure to drop. A second explanation is that the temperature dependence of the thermal capacities or the thermal resistances is not modelled correctly. Finite

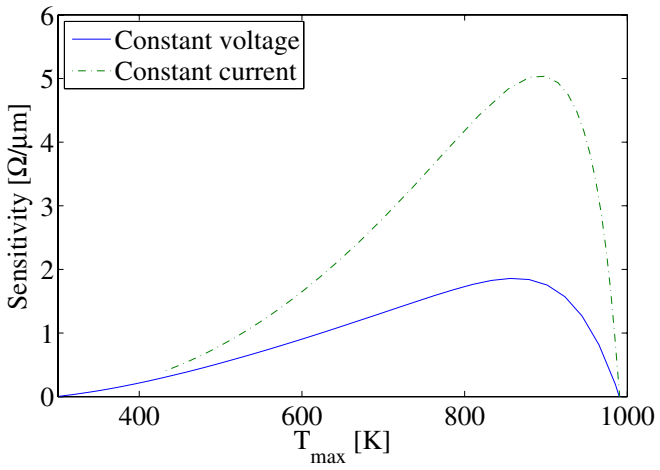

Figure 9. There is a difference between driving the heaters with a constant voltage and with a constant current. The temperature shown on the horizontal axis is the maximum heater temperature at minimum overlap. The maximum sensitivity of the sensor is around 2.7 times higher when a constant current is applied to the sensor. The heaters have the following dimensions: heater width and air gap 3 μm, heater length 610 μm (sensing part 130 μm and legs 240 μm), heater height 50 μm and substrate gap 3 μm. The doping concentration in this simulation is 3.5×10^{18} cm^{-3}.

size effects due to downscaling cannot be the origin of the deviation. In silicon and silicon dioxide layers thicker than 1 μm, finite size effects should be negligible [25, 26], which is the case in our sensors. The thermal conductivity of the air gap suffers from finite size effects on the boundary layer between silicon and air [22]. These boundary effects in fact increase the effective width of the air gap, which would result in a shift of the sensitivity peak in simulation towards lower temperatures. This does not match with our measurements.

The model of the sensor is also used to determine the influence of different operating modes. Two operating modes are (a) applying a constant voltage and measuring the current and (b) applying a constant current and measuring the voltage. Other possibly interesting operating modes, which were not investigated, are controlling the voltage or current in order to create a constant power dissipation or to create a constant heat flow towards the stage, independent of the stage overlap.

The effect of applying a constant voltage or a constant current to the heater structures is shown in figure 9. By applying a constant current to the sensor, the maximum sensitivity is 2.7 times higher than by applying a constant voltage. This can be understood by looking at the equations for power dissipation in the heater structures,

$$P_{\mathrm{U}}(T) = \frac{U^2}{R_{\mathrm{E}}(T)} \tag{8}$$

$$P_{\mathrm{I}}(T) = I^2 R_{\mathrm{E}}(T). \tag{9}$$

If a situation is considered with constant voltage, at minimum overlap the heater will reach a certain (high) temperature and therefore a (high) resistance. If the stage is moved to maximum overlap, the heater structure will cool down and the resistance will decrease. According to (8), this will result in an increase in the power supplied to the sensor. This increase in power increases the heater temperature, which counteracts the decrease in temperature by more stage overlap. If a constant current is chosen, from minimum to maximum overlap, the resistance will decrease and according to (9), the power supplied to the sensor will also decrease, which amplifies the cooling effect of the stage displacement. Applying a constant current can lead to instability when the sensor is operated close to and beyond $S_{\max}$.

The operating mode of the sensor also influences the time it takes for the heater to react to a change in stage position, i.e. the thermal time constant of the heater. When a low heater current or voltage is used, this will lead to a certain low resistance. When a step is made in the supply voltage, the low initial resistance leads to an initial power that is higher than the final power, according to (8). When a step is made in the applied current, the low initial resistance leads to an initial power that is lower than the final power, according to (9). As a result, the temperature of the heater will increase more quickly with a constant supplied voltage than with a constant applied current. Simulations with the lumped model show that the current mode will result in a time constant that is roughly two to three times higher than the time constant in voltage mode.

3. Design

The modelling section, section 2, shows the influence of the parameters such as doping concentration, operating temperature, heater leg length and heater width on the sensitivity of the sensor. Several conclusions can be drawn from modelling.

The doping concentration in the device layer of the SOI wafer does affect the sensitivity of the sensor. Choosing a low doping concentration will result in a sensor with increased sensitivity. For our system, a minimum doping concentration of 1×10^{16} cm^{-3} still is acceptable, based on the increasing electrical time constant when decreasing the doping concentration. For this research, SOI wafers with two different doping concentrations were available: 3.5×10^{18} cm^{-3} and 4.7×10^{18} cm^{-3}.

The sensitivity of the sensor as a function of the operating temperature shows that this function is closely related to the resistivity curve of silicon as a function of temperature. Up to a certain maximum operating temperature set point, the sensitivity will increase. Above this temperature set point, the sensitivity of the sensor will decrease. In this work, the sensor is operated on the positive slope of the sensitivity curve.

The heater width should be chosen as small as possible to result in a sensor with a higher sensitivity. The minimum width of the heaters is restricted by the fabrication process. A minimum feature size of 3 μm is recommended for reliable fabrication. Sensors with designed heater widths of 2 μm and 3 μm have been produced.

Varying the leg length of the heaters will result in a sensitivity curve that has an optimum. For a heater width and air gap of 3 μm, a doping concentration of 3.5×10^{18} cm^{-3}, a device layer thickness of 50 μm, a sensing part length of 130 μm and a substrate gap of 3 μm, the optimum leg length is

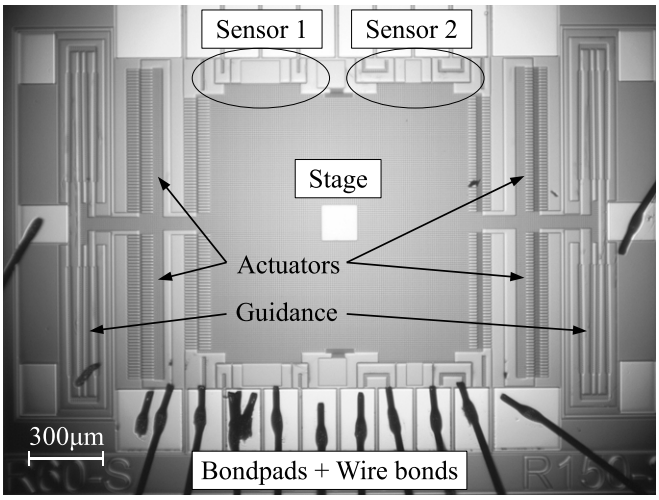

Figure 10. Top view: optical micrograph of the proof of principle system. The comb-drive actuators in combination with the guidance mechanism are able to enable stage displacements up to 30 μm in both directions. Four differential sensors with different geometries are connected to a single stage. Only the two sensor pairs on the top side of the stage are indicated here; two more sensor pairs are located on the bottom side of the stage.

240 μm. Sensors with various leg lengths have been produced. Section 2.5 showed that the sensor should be used in current mode. This means that a constant current is applied to the heaters and that the voltage over the heaters is a measure for the stage position. With the same sensor configuration and depending on the temperature set point, applying a constant current results in a sensitivity that is up to 2.7 times higher than that in voltage mode.

The differential sensor is integrated into the system design. In a first production run, a proof of the sensor principle was given [27, 28]. In this production run, a SOI wafer with device layer 25 μm, oxide layer 1 μm and doping concentration 4.7×10^{18} cm^{-3} was used. The moving stage is actuated using electrostatic comb drives [29]. The stage used folded flexures as a straight guidance mechanism to ensure parallel movement with respect to the heaters. The displacement obtained using the folded flexure straight guidance is limited to roughly 30 μm in both directions. For larger displacements, the stiffness of the guidance mechanism in the direction perpendicular to the direction of motion of the stage is not sufficient to prevent the complete stage from snap-in due to electrostatic forces. This proof-of-principle system is shown in figure 10. Various differential sensors with different heater geometries are connected to a single stage. A gold layer was added to the bondpads to facilitate the connection with the wire bonds.

In a second production run, the straight guidance mechanism using four folded flexures is replaced by two constrained folded flexures [30]. This straight guidance mechanism can reach displacements of up to 100 μm in both directions. A SOI wafer with device layer 50 μm, oxide layer 3 μm and doping concentration 3.5×10^{18} cm^{-3} was used. No gold deposition layer was used in the second production run, but wires were bonded directly onto the silicon.

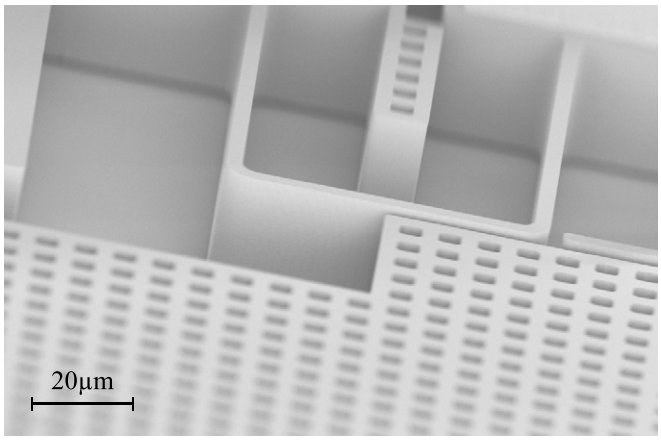

Figure 11. Scanning electron micrograph of a fabricated heater in front of the stage. This heater was part of the first production run, using wafers with a device layer of 25 μm and an oxide layer of 1 μm.

4. Fabrication

For both production runs described in section 3, aspect-ratio-controlled deep reactive-ion etching (DRIE) was used to etch through the full device layer of the wafer. The directional etching and resulting high aspect ratios are particularly useful for good mechanical behaviour of the leaf springs used for straight guiding the stage, resulting in low driving stiffness and high transversal and out-of-plane stiffness. A minimum trench width and a minimum feature size of 3 μm is used in the design, limited by the aspect ratio of the DRIE step and limited by the resolution of the fabrication of the photolithographic masks. A maximum trench width of 50 μm is used to prevent large variations in etch loading. Etch loading influences the etch rate and the subsurface profile development [31]. For this reason, several etch compensation structures are included in the design, as depicted in figure 2. After reactive-ion etching, the structures were released from the substrate by isotropic HF vapour phase etching of the buried oxide layer [32]. Thin structures ($<$10 μm) are released from the substrate in this way. Large structures will stay mechanically fixed to the substrate, while being electrically isolated from the substrate due to the oxide layer. Large bodies that should be floating are perforated to be released from the substrate. The fabricated devices are diced, glued and wire bonded with thin aluminium wires to a printed circuit board for measurement. A scanning electron micrograph of a sensor from the first production run is shown in figure 11.

5. Experiment

In this section, the measurement setups will be described first. Subsequently the sensor output voltage as a function of the displacement, the sensor noise and the time constants of the system will be discussed.

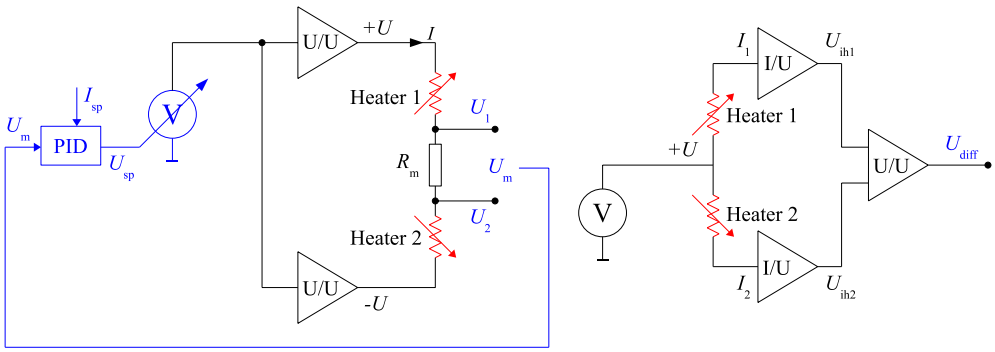

Figure 12. Schematic overview of the measurement setups for current (left) and voltage (right) mode. For constant current, the measured voltage U_m over the resistor R_m is used to determine the current through the heaters. The driving voltage ($+U$ and $-U$) is adjusted to control the current through the heaters (I) using the current set point I_{sp}. The advantage of this half-bridge measurement setup is that the output voltages U_1 and U_2 have little offset and can be directly used for A/D conversion with little quantization noise. For constant voltage, a well-defined constant voltage source is used to drive the heaters. The resulting currents through the heaters (I_1 and I_2) are amplified using two equal current-to-voltage amplifiers. A second, differential amplifier is used to generate the signal (U_{diff}) for A/D conversion. (The digital part of the measurement setup is depicted in blue and the MEMS structures are depicted in red.)

5.1. Measurement setup

Two different measurement setups were developed to characterize the fabricated sensors. One setup applies a constant current and measures the voltage over the heaters, and the other setup applies a constant voltage and measures the current through the heaters. The current control setup (figure 12 (left)) places two heaters in series, so equal current through both heaters is guaranteed. The current through the heaters is measured by the voltage over the low-impedance resistor R_m. The voltage source is adjusted to generate a constant current I through the heaters. The sensor output is the voltage on either of the electrodes of the resistance R_m with respect to ground. The bandwidth of the control loop limits the bandwidth of the sensor in this configuration. The measurement setup for voltage control (figure 12 (right)) is more straightforward but requires more analogue electronics. A voltage supply is directly connected to both heaters in parallel. The resulting currents are amplified in two equal current-to-voltage amplifiers. A differential amplifier is used to generate the measurement signal.

A secondary measurement setup is used to calibrate the stage deflection as a function of the actuation voltage on the comb drives. Stroboscopic video microscopy is used for this purpose, performed with a Polytec MSA-400 and its Planar Motion Analyzer software [33]. The measured data provide accurate information ($1\sigma \sim 20$ nm) about the stage position at a specified actuation voltage. The comb-drive actuators in combination with the flexure-based stage are designed to generate the required 100 μm deflection at a maximum voltage of 80 V.

5.2. Sensor output and noise

At a constant heater current of 9.8 mA, the displacement versus the sensor output voltage was measured and shown in figure 13 (top). The current is chosen such that a maximum heater temperature at minimum overlap of 800 K is expected. The stage movement in this experiment is from -55 μm to +55 μm. The measured voltage U_2 ranges from -0.807 V to +0.758 V. The resistance of heater 1 decreases from 1108 Ω to 963 Ω and the resistance of heater 2 increases from 953 Ω to 1127 Ω. This corresponds to an average sensitivity of 2.91 Ω μm^{-1}.

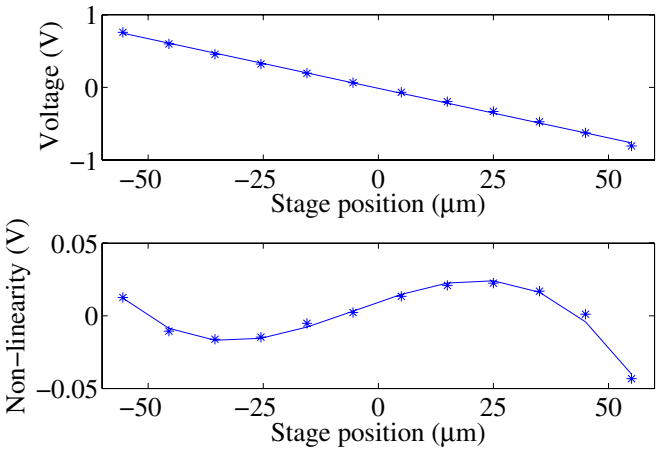

Figure 13. The measured voltage output as a function of the stage displacement is shown for the situation where a constant current of 9.8 mA is applied (top). A linear fit is made with slope -13.7mV μm^{-1} and offset -12.5mV. The deviation from the linear fit can be approximated by a third-order polynomial (bottom). The heaters in this experiment have the following dimensions: heater width and air gap 3 μm, heater length 610 μm (sensing part 130 μm and legs 240 μm), heater height 50 μm and substrate gap 3 μm. The doping concentration of this wafer is 3.5×10^{18} cm^{-3}.

The linear fit through the measured data has a slope of -13.7mV μm^{-1}. The deviation from a linear fit is measured to be at maximum 23 mV, which corresponds to approximately 1.6 μm. Considering all nonlinear effects in the sensor, for instance the electrical resistivity of silicon as a function of the temperature, and the fairly large temperature variation over the sensing part of the heater, the differential sensor is surprisingly linear. The nonlinearity of the sensor is highly repeatable and can be fitted with a third-order polynomial with minor deviation, as shown in figure 13. This is necessary for accurate positioning.

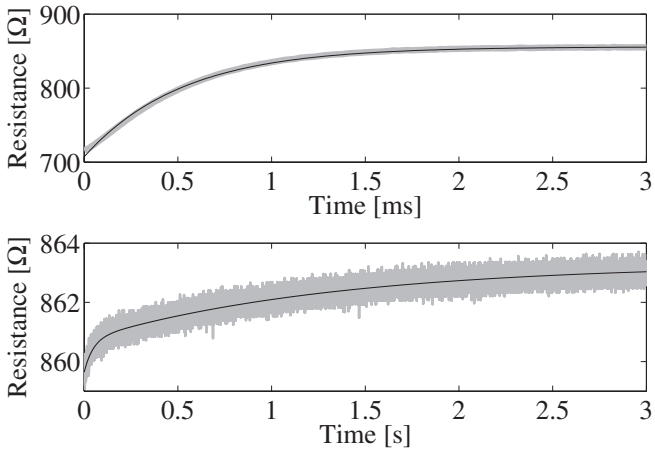

Figure 14. This sensor structure has a time constant τ_{heater} of 522 μs (top). Two more time constants can be distinguished; the stage has a time constant τ_{stage} of 50.8 ms and the complete system has a time constant τ_{system} of 1.32 s (bottom). The measurement results are depicted in light grey and the exponential fits in black. The heaters in this experiment have the following dimensions: heater width and air gap 3 μm, heater length 610 μm (sensing part 130 μm and legs 240 μm), heater height 50 μm and substrate gap 3 μm.

The noise of the unfiltered sensor signal has an RMS value of 122 μV at a sampling frequency of 1 kHz. If the noise is assumed white, this leads to a noise value of 3.9 μV Hz$^{-1/2}$. Using the slope of 13.7 mV μm^{-1}, this yields 0.28 nm Hz$^{-1/2}$. The noise of the measurement setup is dominated by the specified RMS noise of the 16 bit A/D converter, which is 98.1 μV. The measurement signal is digitally filtered with a sixth-order low-pass filter with a cut-off frequency of 25 Hz. The filtered signal has an RMS noise value of 22.2 μV, which corresponds to a sensor resolution of 1.65 nm.

5.3. Time constants and drift

An important drawback of thermal systems is usually the low bandwidth due to high thermal time constants. With a thermal sensing or actuation principle in MEMS, much higher bandwidths can be achieved. The thermal capacitance ($C \sim r^3$) decreases much faster due to miniaturization than the thermal resistance increases ($R \sim r^{-1}$). Therefore, the time constant will decrease quadratically with decreasing size ($\tau = RC \sim r^2$). In order to measure the time response of the heaters, a voltage step was applied to one of the two heaters of the sensor. The resistance of the heater was measured at a high sample rate (see figure 14 (top)). The heater structure has a time constant τ_{heater} of 522 μs, which means that the sensor has a bandwidth (−3 dB) of 305 Hz.

The time constant of the heater structure is not the only time constant in the complete system. By applying a step voltage to the second heater in the sensor and measuring the response on the first heater, two more time constants are found (figure 14 (bottom)). A time constant τ_{stage} of 50.8 ms was found that can be attributed to the time constant of the stage and a time constant τ_{system} of 1.32 s was found that is caused by heating of the complete system and substrate.

Continuous usage of the sensor can prevent τ_{system} from showing up, because the power dissipation of the sensor is more or less constant, independent of stage position, as shown by the simulations in table 1. The stage time constant τ_{stage} is harder to suppress, since at every stage movement the temperature distribution over the stage changes. The influence of the stage time constant can be reduced by choosing an operating mode of the sensor in which the power flow towards the stage for each heater is constant, or by adding a stage position history in the sensor that compensates for the stage time constant. In both cases, information about the model is used to make predictions about the power flows and time constants in the sensor, based on the applied current or voltage and the previously known positions. For control, the relatively large time constant of the stage does not lead to large phase shifts or instability; therefore, the control bandwidth is not limited by the stage bandwidth.

A drift measurement was performed with the differential sensor. Without control of ambient temperature and air humidity, the drift of the sensor was determined to be 32 nm over a measurement period of 32 h. A 'run-in' time of several days was required to remove this long-term drift. Both ambient temperature and air humidity do influence the sensor response. These effects can be compensated for by using a reference sensor with a fixed overlap that purely measures environmental fluctuations. A long-term drift of single heater resistances was observed over a time period of more than 100 h. Even when using the heater at 'reasonable' temperatures, around 600 K, the resistance increases irreversibly with roughly 5% with respect to the initial resistance. For example, thermal oxidation [18] and thermal activation of oxygen [34] are effects that can change the properties of the silicon material slightly. Electromigration and diffusion effects due to fairly high current densities on the wire bond to silicon interface are difficult to predict, but they can also have a significant influence. Frequent internal calibration of the sensor by hard mechanical endstops will be used to compensate for long-term drift effects.

6. Conclusion

This work presents a MEMS displacement sensor based on the conductive heat transfer of a resistively heated silicon structure towards an actuated stage parallel to the structure. Using the heaters in a differential configuration and using a typical sensor design, an RMS position noise of 2 nm was measured. This resolution was measured over a range of 110 μm and after filtering with a bandwidth of 25 Hz. Due to the small scale of MEMS structures, the thermal sensing principle can achieve reasonably high bandwidths, in contrast with thermal systems in the macro world.

A dynamic multiphysics lumped capacitance model was generated to optimize the sensor sensitivity as a function of doping concentration, operating temperature, heater leg length and heater width. The accuracy of the model is within 10% with respect to the measured values on the positive slope of the sensitivity curve. Sensitivity changes due to a variation

in the heater leg length and the heater width can be predicted within the same accuracy.

Based on this model, we conclude that the heater width should be designed as small as allowed by the fabrication process. An optimum in the heater leg length exists but does not have a large influence on the sensitivity. Constant current supplied to the heaters, rather than constant voltage, results in a higher sensitivity. A decrease in doping concentration will also increase the sensitivity of the sensor substantially.

An important conclusion is that the differential sensor can be easily incorporated in a silicon-on-insulator (SOI)-based process, and fabricated within the same mask as electrostatic actuators and flexure-based stages. The sensor including bondpads requires only little wafer surface area ($<$ 0.5 mm^2). With nanometer resolution, the presented thermal displacement sensor is an interesting sensor for accurate positioning systems.

Acknowledgments

The authors would like to thank Joël Geerlings for his help in fabricating the structures. They also thank Jan Leideman, Ali Khiat and Urs Staufer for their support in supervising Richard in his master project. This work is performed in the CLEMPS research project with project number PNE07004, supported by the Dutch association Point-One, which is empowered by the Ministry for Economic Affairs.

References

[1] Hornbeck L J 1997 Digital light processing for high-brightness, high-resolution applications pp 1–14 *Electronic Imaging '97*

[2] Sampsell J B 1994 Digital micromirror device and its application to projection displays *J. Vac. Sci. Technol.* B **12** 3242–6

[3] Binnig G K, Quate C F and Gerber Ch 1986 Atomic force microscope *Phys. Rev. Lett.* **56** 930–3

[4] Kuijpers A A, Krijnen G J M, Wiegerink R J, Lammerink T S J and Elwenspoek M C 2006 A micromachined capacitive incremental position sensor: 1. Analysis and simulations *J. Micromech. Microeng.* **16** S116–24

[5] Kuijpers A A, Krijnen G J M, Wiegerink R J, Lammerink T S J and Elwenspoek M C 2006 A micromachined capacitive incremental position sensor: 2. Experimental assessment *J. Micromech. Microeng.* **16** S125–34

[6] Chu L L and Gianchandani Y B 2003 A micromachined 2D positioner with electrothermal actuation and sub-nanometer capacitive sensing *J. Micromech. Microeng.* **13** 279–85

[7] Bellouard Y, Said A A, Dugan M and Bado P 2005 High accuracy micro-displacement sensor with integrated optics-based detection means *Proc. IEEE Int. Conf. on Robotics and Automation (Barcelona, Spain, April 2005)* pp 850–5

[8] Maluf N and Williams K 2004 *An Introduction to Microelectromechanical Systems Engineering* 2nd edn (Boston, MA: Artech House Publishers)

[9] DiBiasio C M and Culpepper M L 2008 Design of a meso-scale six-axis nanopositioner with integrated position sensing *Proc. Vth Annu. Int. Symp. on Nanomanufacturing (Delft, The Netherlands)*

[10] Lantz M A, Binnig G K, Despont M and Drechsler U 2005 A micromechanical thermal displacement sensor with nanometre resolution *Nanotechnology* **16** 1089–94

[11] Dauderstädt U A, de Vries P H S, Hiratsuka R and Sarro P M 1995 Silicon accelerometer based on thermopiles *Sensors Actuators* A **46** 201–4

[12] Petropoulos A, Kaltsas G and Goustouridis D 2009 A novel system for displacement sensing, integrated on a plastic substrate *Microelectron. J.* **40** 1387–92

[13] Koster M P 2005 *Constructieprincipes voor het nauwkeurig bewegen en positioneren* 4th edn (Enschede, The Netherlands: PPI Uitgeverij)

[14] Meijaard J P, Brouwer D M and Jonker J B 2010 Analytical and experimental investigation of a parallel leaf spring guidance *Multibody Syst. Dyn.* **23** 77–97

[15] 20-sim 2010 http://www.20sim.com/

[16] Incropera F P and DeWitt D P 1996 *Introduction to Heat Transfer* 3rd edn (New York: Wiley)

[17] Glazov V M and Pashinkin A S 2001 The thermophysical properties (heat capacity and thermal expansion) of single-crystal silicon *High Temp.* **39** 413–9

[18] Sze S M and Ng K K 2006 *Physics of Semiconductor Devices* 3rd edn (Hoboken, NJ: Wiley)

[19] Lienhard J H, IV and Lienhard J H, V 2008 *A Heat Transfer Textbook* 3rd edn (Cambridge, MA: Phlogiston Press)

[20] Ravindra N M, Sopori B, Gokce O H, Cheng S X, Shenoy A, Jin L, Abedrabbo S, Chen W and Zhang Y 2001 Emissivity measurements and modeling of silicon-related materials: an overview *Int. J. Thermophys.* **22** 1593–611

[21] COMSOL Multiphysics 2010 http://www.comsol.com/

[22] Durig U 2005 Fundamentals of micromechanical thermoelectric sensors *J. Appl. Phys.* **98** 044906

[23] Dorkel J M and Leturcq P 1981 Carrier mobilities in silicon semi-empirically related to temperature, doping and injection level *Solid-State Electron.* **24** 821–5

[24] Reggiani S, Valdinoci M, Colalongo L, Rudan M, Baccarani G, Stricker A D, Illien F, Felber N, Fichtner W and Zullino L 2002 Electron and hole mobility in silicon at large operating temperatures: bulk mobility *IEEE Trans. Electron. Devices* **49** 490–9

[25] Asheghi M, Behkam B, Yazdani K, Yoshi R and Goodson K 2002 Thermal conductivity model for thin silicon-on-insulator layers at high temperatures *Proc. 2002 IEEE Int. SOI Conf. (Williamsburg, VA, USA, Oct. 2002)* pp 51–2

[26] Yamane T, Nagai N, Katayama S and Todoki M 2002 Measurement of thermal conductivity of silicon dioxide thin films using a 3ω method *J. Appl. Phys.* **91** 9772–6

[27] Hogervorst R P, Krijnen B, Brouwer D M, Engelen J B C and Staufer U 2010 A single-mask thermal displacement sensor in MEMS *Proc. 10th EUSPEN Int. Conf. (Delft, The Netherlands)* vol 1, pp 47–50

[28] Krijnen B, Hogervorst R P, Van Dijk J W, Engelen J B C, Brouwer D M and Abelmann L 2010 Single-mask thermal displacement sensor in MEMS *Proc. MME 2010 Int. Workshop (Enschede, The Netherlands)* pp 52–55

[29] Legtenberg R, Groeneveld A W and Elwenspoek M C 1996 Comb-drive actuators for large displacements *J. Micromech. Microeng.* **6** 320–9

[30] Brouwer D M, Otten A, Engelen J B C, Krijnen B and Soemers H M J R 2010 Long-range elastic guidance mechanisms for electrostatic comb-drive actuators *Proc. 10th EUSPEN Int. Conf. (Delft, The Netherlands)* vol 1, pp 462–5

[31] Jansen H V, de Boer M J, Unnikrishnan S, Louwerse M C and Elwenspoek M C 2009 Black silicon method X: a review on high speed and selective plasma etching of silicon with profile control: an in-depth comparison between bosch and cryostat DRIE processes as a roadmap to next-generation equipment *J. Micromech. Microeng.* **19** 1–41

[32] Holmes P J and Snell J E 1966 A vapour etching technique for the photolithography of silicon dioxide *Microelectron. Reliab.* **5** 337–41

[33] Polytec 2010 http://www.polytec.com/

[34] Cazcarra V and Zunino P 1980 Influence of oxygen on silicon resistivity *J. Appl. Phys.* **51** 4206–11